ADVANCES IN ATMOSPHERIC SCIENCES, VOL. 39, AUGUST 2022, 1343–1359

• **Original Paper** •

Decadal Methane Emission Trend Inferred from Proxy GOSAT XCH_4 Retrievals: Impacts of Transport Model Spatial Resolution※

Sihong ZHU[1,4], Liang FENG[*2,3], Yi LIU[*1], Jing WANG[1], and Dongxu YANG[1]

[1]*Carbon Neutrality Research Center*, *Institute of Atmospheric Physics*, *Chinese Academy of Sciences*, *Beijing* 100029, *China*

[2]*National Centre for Earth Observation*, *University of Edinburgh*, *Edinburgh*, *EH*9 3*FF*, *UK*

[3]*University of Edinburgh*, *Edinburgh*, *EH*9 3*FF*, *UK*

[4]*University of Chinese Academy of Sciences*, *Beijing* 100049, *China*

(Received 19 December 2021; revised 22 April 2022; accepted 25 April 2022)

ABSTRACT

In recent studies, proxy XCH_4 retrievals from the Japanese Greenhouse gases Observing SATellite (GOSAT) have been used to constrain top-down estimation of CH_4 emissions. Still, the resulting interannual variations often show significant discrepancies over some of the most important CH_4 source regions, such as China and Tropical South America, by causes yet to be determined. This study compares monthly CH_4 flux estimates from two parallel assimilations of GOSAT XCH_4 retrievals from 2010 to 2019 based on the same Ensemble Kalman Filter (EnKF) framework but with the global chemistry transport model (GEOS-Chem v12.5) being run at two different spatial resolutions of 4° × 5° (R4, lon × lat) and 2° × 2.5° (R2, lon × lat) to investigate the effects of resolution-related model errors on the derived long-term global and regional CH_4 emission trends. We found that the mean annual global methane emission for the 2010s is 573.04 Tg yr^{-1} for the inversion using the R4 model, which becomes about 4.4 Tg yr^{-1} less (568.63 Tg yr^{-1}) when a finer R2 model is used, though both are well within the ensemble range of the 22 top-down results (2008–17) included in the current Global Carbon Project (from 550 Tg yr^{-1} to 594 Tg yr^{-1}). Compared to the R2 model, the inversion based on the R4 tends to overestimate tropical emissions (by 13.3 Tg yr^{-1}), which is accompanied by a general underestimation (by 8.9 Tg yr^{-1}) in the extratropics. Such a dipole reflects differences in tropical–mid-latitude air exchange in relation to the model's convective and advective schemes at different resolutions. The two inversions show a rather consistent long-term CH_4 emission trend at the global scale and over most of the continents, suggesting that the observed rapid increase in atmospheric methane can largely be attributed to the emission growth from North Africa (1.79 Tg yr^{-2} for R4 and 1.29 Tg yr^{-2} for R2) and South America Temperate (1.08 Tg yr^{-2} for R4 and 1.21 Tg yr^{-2} for R2) during the first half of the 2010s, and from Eurasia Boreal (1.46 Tg yr^{-2} for R4 and 1.63 Tg yr^{-2} for R2) and Tropical South America (1.72 Tg yr^{-2} for R4 and 1.43 Tg yr^{-2} for R2) over 2015–19. In the meantime, emissions in Europe have shown a consistent decrease over the past decade. However, the growth rates by the two parallel inversions show significant discrepancies over Eurasia Temperate, South America Temperate, and South Africa, which are also the places where recent GOSAT inversions usually disagree with one other.

Key words: methane emissions, long-term trend, horizontal resolution

Citation: Zhu, S. H., L. Feng, Y. Liu, J. Wang, and D. X. Yang, 2022: Decadal methane emission trend inferred from proxy GOSAT XCH4 retrievals: Impacts of transport model spatial resolution. *Adv. Atmos. Sci.*, **39**(8), 1343−1359, https://doi.org/10.1007/s00376-022-1434-6.

Article Highlights:

- Inversion modeling systems using CTMs with coarse horizontal resolutions can reliably estimate global total methane emissions and give a rather credible long-term trend in all TransCom-3 regions except for Eurasia Temperate, South America Temperate, and South Africa.
- Emission increases in North Africa and South American Temperate contributed the most strongly to global emission growth from 2010 to 2014. During the second half of the 2010s, accelerated methane increases in the atmosphere were mainly driven by Eurasia Boreal and Tropical South America emissions.

※ This paper is a contribution to the special issue on Carbon Neutrality: Important Roles of Renewable Energies, Carbon Sinks, NETs, and non-CO_2 GHGs.

* Corresponding authors: Yi LIU, Liang FENG
Emails: liuyi@mail.iap.ac.cn, liang.feng@ed.ac.uk

- There are large uncertainties and debates in methane emission from Eurasia Temperate. We discuss possible causes for different emission estimates, particularly over China, to highlight the adverse effects of the model transport error over regions that are poorly constrained by observations or a priori estimates.

1. Introduction

Methane concentrations in the atmosphere have more than doubled since the pre-industrial era, contributing about 20% to present-day human-induced global warming (Myhre et al., 2013; Etminan et al., 2016). Methane is also a chemical precursor to tropospheric ozone, which has adverse effects on both human and ecosystem health. Its lifetime in the atmosphere is about 8 to 11 years (Patra et al., 2011; Prather et al., 2012Canadell et al., 2021). Quantifying methane emission and understanding the factors driving its interannual variations are of both the public and scientific interest because CH_4 emission reduction is now considered to be an efficient strategy for combating global warming, which can improve air quality (Shindell et al., 2012; Schaefer et al., 2016; Schaefer, 2019).

Surface observations from the NOAA network (Dlugokencky, NOAA/GML (gml.noaa.gov/ccgg/trendsch4/) reveal significant interannual variability in the rate by which methane is increasing. This variability is caused by an imbalance of surface emissions and atmospheric sinks, mainly due to reactions with hydroxyl radicals (OH), chlorine atoms (Cl), and excited atomic oxygen (O(1D)) (Saunois et al., 2020). Emissions can be broadly divided into natural (e.g., wetlands, inland water systems, geological seeps, termites, oceans, terrestrial permafrost, and hydrates) (Bloom et al., 2010; Kirschke et al., 2013; Melton et al., 2013) and anthropogenic sources (e.g., from agriculture, fossil fuel combustion, and waste management) (Kirschke et al., 2013; Schaefer, 2019; Saunois et al., 2020). It is challenging to quantify the methane budget accurately and determine the drivers for the unstable methane trend due to large uncertainties in both sources (emissions) and sinks (Canadell et al., 2021). In the past several years, many studies focused on the reasons for the plateau in the trend and subsequent regrowth of CH_4 in the 2000s but reached no consensus, which is discussed in detail and concluded by Canadell et al. (2021). Based on sectoral a priori emission inventories derived from "Bottom-up" approaches, the "Top-down" method takes advantage of atmospheric measurements to optimize the total emissions and sinks (Jacob et al., 2016; Brasseur and Jacob, 2017). The quality of inferred emissions depends critically on the quality and density of measurements. In the 2010s, long-term satellite retrievals from GOSAT and TROPOMI, with improved precision and accuracy, provided worldwide measurements to cover spatial and temporal changes in the atmospheric column-averaged concentration of (XCH_4) to constrain and interpret the interannual variation of global and regional methane emissions and their trends (Fraser et al., 2013, 2014; Wecht et al., 2014; Turner et al., 2015; Feng et al., 2017; Lunt et al., 2019, 2021; Maasakkers et al., 2019; Miller et al., 2019). In the processes of "Top-down" inverse modeling, atmospheric transport and chemistry models (CTMs), driven by meteorological fields, act as a "bridge" to link methane sources and sinks to atmospheric concentrations and thus also impact the inversion results.

Several studies have investigated the influence of observations from different platforms such as in-situ measurements and remotely-sensed retrievals, uncertainties in prior emissions, and other inversion parameters in observationally-based system simulation experiments (OSSEs) (Meirink et al., 2008; Eraser et al., 2014; Bousserez et al., 2016; Turner et al., 2018; Zhang et al., 2018; Lu et al., 2021). However, errors in the atmospheric models used to simulate CH4 remain poorly characterized (Saito et al., 2013; Locatelli et al., 2015). These errors are mainly derived from transport errors and horizontal resolution-related representative or observation mismatch errors (Ganesan et al., 2019; Stanevich et al., 2020, 2021). Transport errors contain biases in numerical convective and advective schemes (Strahan and Polansky, 2006; Saito et al., 2013; Yu et al., 2018; Bisht et al., 2021), meteorological fields (Locatelli et al., 2013, Pandey et al., 2019), and parametrization of subgrid-scale processes (Locatelli et al., 2015). Saito et al. (2013) compared vertical profiles of twelve chemistry models in the TransCom-CH_4 intercomparison experiment with aircraft measurements. They concluded that transport uncertainties partly cause the disparity of the vertical gradients among models. Yu et al. (2018) investigated the impact of model resolution on transport in GEOS-Chem using ^{222}Rn, ^{210}Pb, and ^{7}Be tracers. They found that vertical transport is reduced in the model with coarse resolution. Bisht et al. (2021) suggested models at low resolution are probably transporting mass faster in the lower stratosphere, from the tropics to the mid-high latitudes. Influences of these transport errors on methane emissions inversion are also investigated. Locatelli et al. (2015) tested the sensitivity of methane budget to LMDz sub-grid-scale physical parameterizations. They found that the inversions using a coarser version of the transport model are actually masking a poor representation of the stratosphere–troposphere methane gradient in the model. Representative or observational mismatch errors due to model output in coarse grids have geographically broader average values than finer grids. These systematic uncertainties may cause an overestimation or underestimation of anthropogenic emissions related to geographically localized processes (such as oil and gas production and coal mining, biomass burning, livestock, and landfills) (Ganesan et al., 2019).

Stanevich et al. (2020, 2021) focused on short-term biases in the global GEOS-Chem chemical transport model at different model grids and assessed their effects on inversion results. Their simulations using two different spatial resolutions show large differences in the modeled CH_4 column abundances over major source regions such as China. They concluded that the simulation at a higher spatial resolution yielded a better agreement with observations.

To investigate the impacts of the horizontal resolution of CTMs on estimates of global and regional methane emission long-term trends, we report the first comparison of decadal methane emission trends (2010–19) obtained using the same Ensemble Kalman Filter (EnKF, Feng et al., 2017), but with the CTM (GEOS-Chem v12.5) being run at two different spatial resolutions: 4° (lat) × 5° (lon) (Referred to R4 hereafter) versus 2° × 2.5° (Referred to R2 hereafter). Here, a 10-year record of satellite column observations of methane from the Japanese Greenhouse gases Observing SATellite (GOSAT) retrievals was used to constrain the two parallel inversions.

We provide a detailed description of these data in section 2 and a description of the ensemble Kalman filter method and GEOS-Chem model. Validation results obtained using the Total Carbon Column Observing Network (TCCON) measurements are provided in section 3. We report our comparison results in section 4 and provide conclusions in section 5.

2. Data and Methods

2.1. *Ensemble Kalman Filter Inversion Method*

To constrain and optimize past methane fluxes, we utilized an existing Ensemble Kalman Filter (EnKF) framework developed by Feng et al. (2009, 2017) to assimilate space-based measurements of atmospheric concentrations from 2010 to 2019. As detailed by Feng et al. (2017), *a posteriori* methane flux estimates at a location x and time t are assumed to take the form of:

$$f_{\mathrm{p}}^{\mathrm{g}}(x,t) = f_0^{\mathrm{g}}(x,t) + \sum_{i=1}^{n} c_i^{\mathrm{g}} \mathrm{BF}_i^{\mathrm{g}}(x,t) \,, \tag{1}$$

where g denotes the methane tracer gas and $f_0^{\mathrm{g}}(x,t)$ describes a priori emission inventories. The coefficient c_i^{g} represents adjustment parameters for estimating methane fluxes from a joint state vector c through an optimized fitting of the model results to observations. The pulse-like basis function $\mathrm{BF}_i^{\mathrm{g}}(x,t)$ in (1) represents the methane flux perturbations from various sectors across predefined geographic regions. We divided a priori methane inventories into two source categories: anthropogenic and natural emissions. We defined 92 land sub-regions by dividing the 11 TransCom-3 (Gurney et al., 2002) land regions into almost four equal sub-regions, except for China, which was divided into 37 sub-regions due to its large emissions. The 11 oceanic regions defined in the TransCom-3 experiment were combined due to the insignificant exchange between the ocean and atmosphere. We selected state vectors as the monthly coefficients for scaling the pulse-like regional methane fluxes (basis functions) in 93 global regions. To achieve higher spatial resolution for assimilation, in this study, $\mathrm{BF}_i^{\mathrm{g}}(x,t)$ denotes the perturbation of total a priori estimates in various sub-regions for each month, rather than a priori fluxes from different emission sectors as described in Feng et al. (2017). Therefore, we estimated a total of 22 320 (i.e., 2 × (sub-sources) × 93 (sub-regions) × 120 (months)) coefficients through an optimal fitting of model concentrations with observations as follows:

$$\boldsymbol{c}_{\mathrm{a}} = \boldsymbol{c}_{\mathrm{f}} + \boldsymbol{K}\left[\boldsymbol{y} - \boldsymbol{H}(\boldsymbol{c}_{\mathrm{f}})\right] \,, \tag{2}$$

where $\boldsymbol{c}_{\mathrm{f}}$ and $\boldsymbol{c}_{\mathrm{a}}$ denote the a priori and *a posteriori* state vectors, respectively. $\boldsymbol{y}$ represents the XCH_4 observations retrievals by GOSAT in this study, and $\boldsymbol{H}(\boldsymbol{c}_{\mathrm{f}})$ represents a priori information, including the simulation process of the GEOS-Chem relating a priori inventories to concentration fields, as well as the sampling processes from fields to XCH_4 consistent with the format of the observations.

In the ensemble Kalman filter framework, we approximate the a priori error covariance $\boldsymbol{P}_{\mathrm{f}}$ by introducing an ensemble of perturbation states $\Delta\boldsymbol{C}_{\mathrm{f}} = \left[\Delta c_{\mathrm{f}_1}, \Delta c_{\mathrm{f}_2}, \ldots, \Delta c_{\mathrm{f}_{\mathrm{ne}}}\right]$, so that a priori covariance $\boldsymbol{P}_{\mathrm{f}}$ can be described as $\Delta\boldsymbol{C}_{\mathrm{f}}(\Delta\boldsymbol{C}_{\mathrm{f}})^{\mathrm{T}}$. The Kalman gain matrix $\boldsymbol{K}$ in (2) is given by:

$$\boldsymbol{K} \approx \Delta\boldsymbol{C}_{\mathrm{f}}\Delta\boldsymbol{Y}^{\mathrm{T}}\left[\Delta\boldsymbol{Y}(\Delta\boldsymbol{Y})^{\mathrm{T}} + \boldsymbol{R}\right]^{-1} \,, \tag{3}$$

where $\boldsymbol{R}$ is the observation error covariance, and $\Delta\boldsymbol{Y}$ denotes the projection of the flux perturbation ensemble $\Delta\boldsymbol{C}_{\mathrm{f}}$ to observation space $[\Delta\boldsymbol{Y} = \boldsymbol{H}(\Delta\boldsymbol{C}_{\mathrm{f}})]$. The *a posteriori* estimate uncertainties are also in the form of a perturbation ensemble, which can be obtained by introducing a transform matrix $\boldsymbol{T}$:

$$\Delta\boldsymbol{C}_{\mathrm{a}} = \Delta\boldsymbol{C}_{\mathrm{f}}\boldsymbol{T} \,, \tag{4}$$

$$\boldsymbol{T}(\boldsymbol{T})^{\mathrm{T}} = \boldsymbol{I} - (\Delta\boldsymbol{Y})^{\mathrm{T}}\left[\Delta\boldsymbol{Y}(\Delta\boldsymbol{Y})^{\mathrm{T}} + \boldsymbol{R}\right]^{-1}\Delta\boldsymbol{Y} \,. \tag{5}$$

For simplifying the calculation of $\boldsymbol{T}(\boldsymbol{T})^{\mathrm{T}}$, we used singular value decomposition (SVD) of the scaled model observation ensembles $\Delta\boldsymbol{Y}^{\mathrm{T}}\boldsymbol{R}^{-1/2}$ and an efficient numerical lower-upper solver to sequentially calculate the *a posteriori* estimates $\boldsymbol{c}_{\mathrm{a}}$ and the associated uncertainties $\Delta\boldsymbol{C}_{\mathrm{a}}$.

2.2. *GEOS-Chem Atmospheric Chemistry and Transport Model*

We used v12.5.0 of GEOS-Chem to describe the relationship between surface emissions and the atmospheric methane distributions, forming part of the forward model in our inversion system. The model is driven by MERRA-2 meteorological re-analysis fields from the Global Modeling and Assimilation Office (GMAO) of NASA (Bosilovich et al., 2016). In our experiments, GEOS-Chem model simulations are run at two horizontal resolutions, at R4 and R2, for comparison. We used 47 hybrid-sigma levels from the surface to 0.01 hPa, of which 30 lie below the dynamic troposphere. We used the non-local boundary layer mixing scheme imple-

mented by Lin and McElroy (2010). The initial CH_4 field on 1 January 2010 was obtained from Feng et al. (2017) with an additional 1-year spin-up period starting in 2009.

We used existing methane inventories for various source types. Specifically, we used the EDGAR v4.3.2 global emission inventory for 2012 [https://edgar.jrc.ec.europa.eu/, last access: 1 December 2017; (Janssens-Maenhout et al., 2019)] to represent anthropogenic emissions. This inventory includes various emission sources related to human activities (coal mining, oil and gas industry, livestock, and waste). We used the United States Environmental Protection Agency inventory (Maasakkers et al., 2016) for the United States and the oil and gas emissions from Sheng et al. (2017) for Canada and Mexico. Additionally, 10-year daily global open fire emissions were obtained from QFED (Darmenov and da Silva, 2013). Monthly wetland emissions from 2010 to 2019 were obtained from the WetCHARTS v1.0 extended ensemble mean (Bloom et al., 2017). For termite emissions, we used the results of Fung et al. (1991). Emissions from geological macro seeps were obtained from Etiope (2015) and Kvenvolden and Rogers (2005). In terms of areal seepage, we used sedimentary basins (micro seepage) and potential geothermal seepage maps from Kvenvolden and Rogers (2005) and emission factors from Lyon et al. (2015).

For the atmospheric sinks of methane, we used a 3-D global tropospheric OH fields based on a GEOS-Chem 1-year full-chemistry simulation to describe the main tropospheric removal process of CH_4 (Fraser et al., 2014). Another tropospheric oxidation sink from Cl atoms is based on fields from Sherwen et al. (2016). The soil uptake calculation uses fields from Fung et al. (1991) with temperature-based seasonality based on Murray et al. (2012). Other minor loss terms in stratospheric oxidation are described by Ridgwell et al. (1999).

2.3. *Data*

GOSAT was launched in 2009 by the Japanese Space Agency (JAXA) in collaboration with the Japanese National Institute for Environmental Studies and the Ministry of Environment. This satellite is equipped with a high-resolution Fourier-transform spectrometer (TANSO-FTS), which enables the measurement of concentrations of both CO_2 and CH_4. GOSAT is in a sun-synchronous orbit, with a local equator crossing time of 1300 LST. The instrument has a ground footprint diameter of 10.5 km with a pixel spacing of approximately 250 km. GOSAT achieves approximate global coverage in three days. We used the v9 GOSAT proxy column methane data from the University of Leicester, including nadir observations over land and glint observations over the ocean from 2009 to 2019 (Parker et al., 2015, 2020), with only the nadir measurements used for inversion. These data are routinely validated against ground-based remote sensing data (Parker et al., 2015) and occasionally with aircraft data (Webb et al., 2016). The proxy retrieval simultaneously provides CH_4 and CO_2 column estimates using absorption features around the wavelength of 1.6 μm, which is most sensitive to changes in these gases in the lower troposphere. In taking the ratio of these retrieved columns, CH_4/CO_2, CO_2 is assumed to be a proxy for modification along the light path (Frankenberg et al., 2011); this minimizes the influence of common factors affecting the retrieval of both gases, e.g., clouds and atmospheric scattering. As a result, this proxy retrieval method is less sensitive to scattering than the traditional full-physics retrieval approach and, therefore, yields greater data density over geographical regions with substantial aerosol loading, e.g., tropical areas during the dry season, when biomass burning is prevalent. Previous analyses have shown that these retrievals have a bias of 0.2% and a single-sounding precision of about 0.72% (Parker et al., 2011, 2015, 2020). We assume that GOSAT proxy column methane has an uncertainty of 1.2% to account for all possible errors, including observational errors, representative errors, and retrieval errors from the radiative transfer model.

3. Validation

3.1. *Comparison with GOSAT retrievals*

Figure 1 presents latitudinal differences between GOSAT-observed XCH_4 values, and simulated using GEOS-Chem with a priori emissions at R4 (a) and R2 (b) model grids, and values obtained using *a posteriori* emissions from (c) the R4 inversion and (d) R2 inversion. In the appendix, Fig. A2 presents the distribution of decadal mean differences. Before inversion, large gaps existed between GOSAT observations and model simulations at the two model grids, especially over mid-latitude and high-latitude areas of the northern hemisphere (NH). These gaps increase over time, reaching over 60 ppbv for the R4 simulation and almost 80 ppbv for the R2 simulation in 2019. After the assimilation of GOSAT measurements, differences between observations and model outputs were reduced to within ±2 ppbv in all latitudinal zones, except for high-latitude regions in the NH and southern hemisphere (SH). The R2 inversion performs better at high latitudes than the R4 experiment, narrowing differences to within ±2.5 ppbv throughout most time periods.

3.2. *Validation using TCCON measurements*

The TCCON is a global network of ground-based Fourier-transform spectrometers. It measures direct solar spectra in the near-infrared spectral region to collect information about atmospheric trace gases, including methane (Wunch et al., 2011). Currently, the TCCON consists of 26 operational stations. Due to their high precision and accuracy, TCCON datasets are commonly used to evaluate satellite retrievals (Karion et al., 2010). Therefore, these datasets provide essential information for comparison with *a posteriori* fields simulated by GEOS-Chem with R4 and R2 grids. The latest GGG2014 release (updated in August 2021) includes 35 long-term datasets of measurements, of which 34 datasets (Fig. A1 in the Appendix) representing the period from 2010 to 2019 were used for validation.

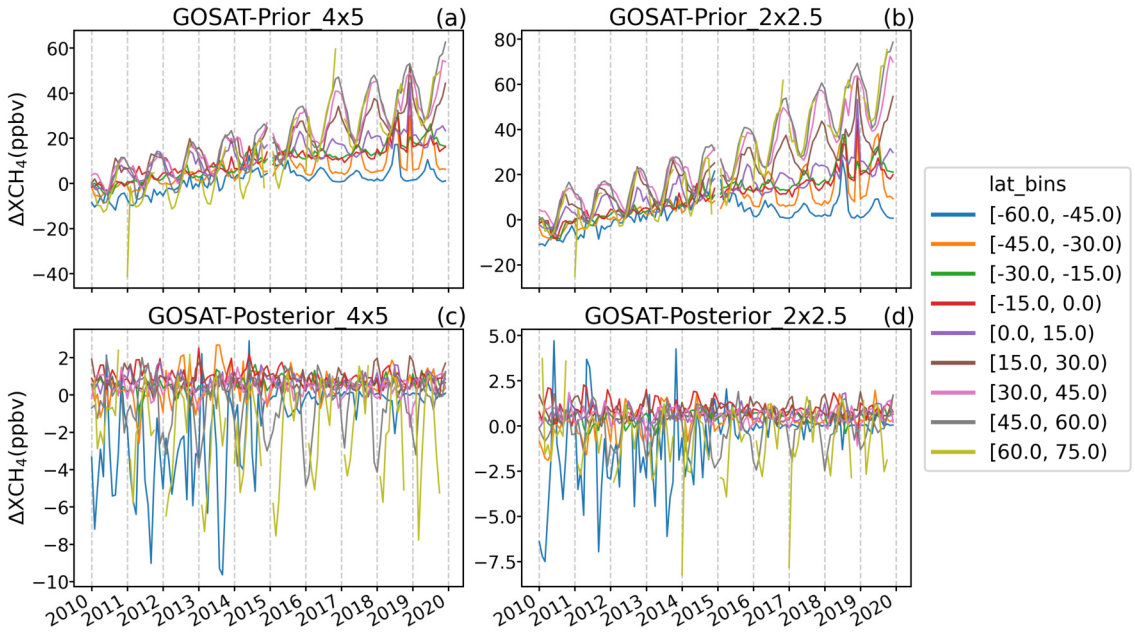

Fig. 1. Latitudinal difference between GOSAT-observed methane column concentrations (XCH_4) and those simulated using GEOS-Chem with a priori emissions at R4 (a) and R2 (b) and using *a posteriori* emissions after inversion at R4 (c) and R2 (d).

Figure 2 presents Taylor diagrams comparing TCCON measurements with GEOS-Chem outputs before and after inversion. Compared with R4 outputs using a priori emissions, we found a weaker correlation of R2 a priori model outputs with TCCON observations. Additionally, the root-mean-square deviation (RSMD) revealed that biases at most stations are larger at the R2 than at the R4 grid. However, the *a posteriori* model outputs of R2 performed better than R4 results, regardless of a correlation coefficient or RSMD. Moreover, compared with a priori outputs, seasonal variations (represented by the standard deviation) of *a posteriori* model results for both grids were closer to the average value of TCCON measurements. Emissions at high latitudes have larger seasonal variations and thus larger standard deviations. Thus, we confirmed that GOSAT retrievals provide useful constraints for a priori methane emissions, and the CTM with higher horizontal resolution performs better in inversion.

4. Results and Discussion

4.1. *Global methane emission trends*

Mean global annual methane emissions in R4 inversion is 573.04 Tg yr^{-1}, compared to 568.63 Tg yr^{-1} for R2 inversion (Table 1). The difference of about 4.4 Tg yr^{-1} is less than 1% of the mean annual emissions. Compared with other inversion results using GEOS-Chem runs at the R4 grid, we found that our results (561.10 Tg yr^{-1} for R4 and 559.91 Tg yr^{-1} for R2) are about 3% higher than the 2010–15 mean methane emission of 546 Tg yr^{-1} estimated by Maasakkers et al. (2019). Lu et al. (2021) also used GEOS-Chem simulations at the R4 grid to conduct GOSAT-only, in-situ-only, and joint GOSAT and in-situ inversions; our results are close to their joint inversion result (551 Tg yr^{-1}) for 2010–17 but much higher than their GOSAT-only inversion. Zhang et al. (2021) expanded the study period from 2017 to 2018 and concluded that the 9-year annual total emissions were 512 Tg yr^{-1} when only GOSAT retrievals were assimilated in inversion. Sensitivity tests (not included) show that the large differences are mainly due to different model OH concentrations. Zhao et al. (2020) studied the influence of the production and loss processes of OH on CH_4 lifetime and the global methane budget on decadal scales and found that interannual variation of OH has a significant impact on the top-down inversion of the methane budget, especially for tropical regions. However, Yin et al. (2021) compared six inversion results optimized by the inversion system PYVAR-LMDz based on the LMDz-INCA (1.9° × 3.75°) CTM (OH fields are from a full chemistry simulation by model LMDZ-INCA and the TransCom model intercomparison experiment). They suggested that the XCH_4 accelerated growth could be mostly induced by increased emissions. Our decadal mean emissions are close to the upper bound (510–570 Tg yr^{-1}) of the 8-year mean values for their six ensemble results. Janardanan et al. (2020) used GOSAT and surface measurements to optimize methane a priori estimates in the NIES-TM-FLEXPART-VAR (NTFVAR) inverse modeling system. They estimated the global annual mean methane emissions to be 573.4 Tg yr^{-1} from 2011 to 2017. Chandra et al. (2021) assimilated surface measurements from NOAA over three decades from 1988 to 2016 and reported global emissions over 2007–16

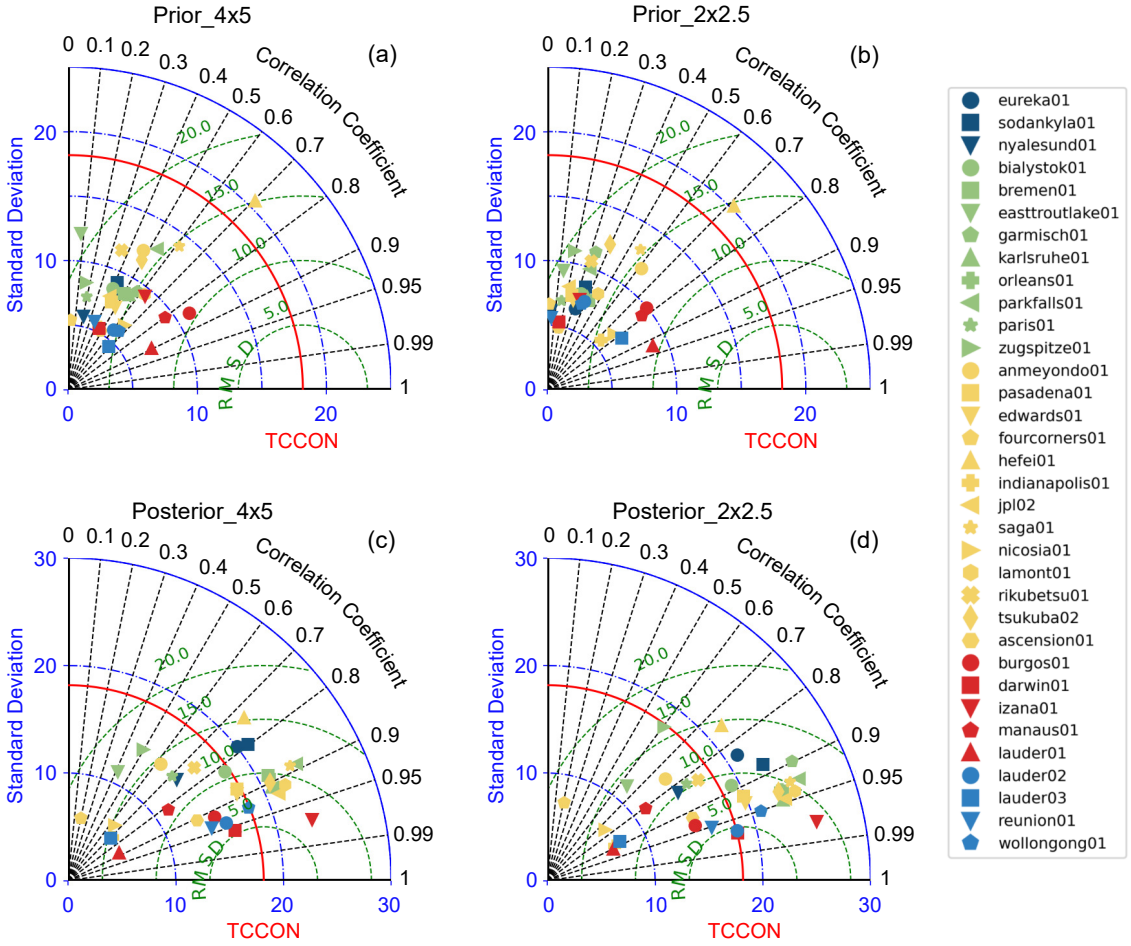

Fig. 2. Taylor diagrams of statistical results [correlation coefficient, standard deviation, and root-mean-square deviation (RMSD)] between surface-measured methane column concentrations (XCH_4) from the TCCON network and those simulated using GEOS-Chem with a priori emissions at R4 (a) and R2 (b), and using *a posteriori* emissions after inversion at R4 (c) and R2 (d) (Deep blue: latitudes of TCCON sites are larger than 60°N; Green: the latitudes of sites are within 45°–60°N; Yellow: the latitudes of sites are within 30°–45°N; Red: the latitudes of sites are within –15°S–45°N; Blue: The sites located in the mid-latitudes of SH).

(renewed growth of atmospheric methane) of 543± 16 Tg yr^{-1}.Based on an ensemble of 22 top-down methane budgets from 2008 to 2017, the Global Carbon Project (GCP) reports that the decadal mean emissions range from 550 to 594 Tg $yr^{-1,}$ with a mean value of 576 Tg yr^{-1}. Among the ensemble members, the 11 GOSAT-only or GOSAT and in-situ joint inversion results range from 564.1 to 594.1 Tg yr^{-1} with mean emissions of 579 Tg yr^{-1} (Saunois et al., 2020). Our results, using two different model grids, are comparable to these 11 GOSAT-related inversions. Several inversion results, including 9 surface CH_4 and 10 satellite XCH_4 inversions reported by Saunois et al. (2020), three decadal inversion results (1988–2016) using surface measurements from 19 sites given by Chandra et al. (2021) as well as global total emissions (Bousquet et al., 2006) were summarized in latest IPCC AR6 report (Canadell et al., 2021). Global total emissions in two inversions using surface CH_4 measurements show similar trends from 2000 to 2017 but large discrepancies in 2015. While continued methane growth occurred in 2015 with anomalies close to 25 Tg yr^{-1} [relative to 2010–16 as given by Chandra et al. (2021)], nine ensemble mean emissions from Saunois et al. (2020) show a plateau after the substantial increase in 2014. These two inversions both show declining trends after 2015, when the ensemble mean result from 10 satellite inversions differs greatly with ongoing increases. Two trends in our inversions are similar to the ensemble mean trend from satellite inversions with sustained growth from 2010 to 2017. The discrepancy between the surface inverted trends and satellite assimilated trends after 2015 still needs further investigation.

Figure 3a presents interannual variations of the global emissions from 2010 to 2019. Long-term increases can be found in both inversions, with the growth rate being 4.95 Tg yr^{-2} in R4 and 3.10 Tg yr^{-2} in the R2 model. The growth rate shows temporal fluctuations, with the largest increase in 2013 (25.51 Tg yr^{-2} in R4 and 13.00 Tg yr^{-2} in R2). Generally, most increases are derived from enhance-

Table 1. Global annual total emissions during the 2010s (Tg yr^{-1}).

Institution	CTM	Gridded (lon×lat)	Period	Observation used	Global total emissions	References
IAP	GEOS-Chem	4° × 5°	2010–19	GOSAT	573.04	this study
		2° × 2.5°			568.63	
University of Harvard	GEOS-Chem	4° × 5°	2010–15	GOSAT	546±2	(Maasakkers et al., 2019)
University of Harvard	GEOS-Chem	4° × 5°	2010–17	GOSAT	515	(Lu et al., 2021)
				In-situ	504	
				GOSAT & in-situ	551	
University of Harvard	GEOS-Chem	4° × 5°	2010–18	GOSAT	512	(Zhang et al., 2021)
JAMSTEC	MIROC4-ACTM	2.8125° × 2.8125°	2007–16	In-situ	543±16	(Chandra et al., 2021)
LSCE/CEA	LMDz-INCA	3.75°×1.875°	2010–17	GOSAT	510–570	(Yin et al., 2021)
NIES	NIES-TM v08.1i	2.5°	2011–17	GOSAT & in-situ	573.4	(Janardanan et al., 2020)
LSCE/IPSL	22 inversions ensemble mean		2008–17	In-situ or GOSAT or GOSAT &in-situ	576 (550–594)	(Saunois et al., 2020)
	11 inversions ensemble mean			GOSAT or GOSAT&in-situ	579 (564–594)	

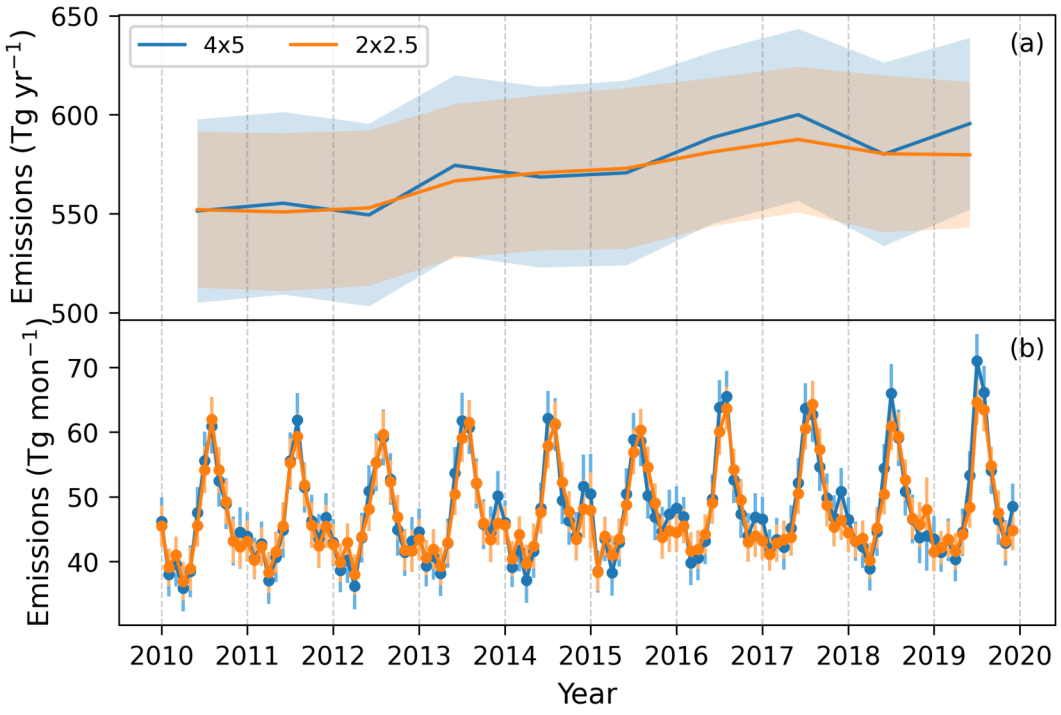

Fig. 3. Annual mean variations of global total methane emissions (a) in R4 (blue) and R2 (orange) versions of the GEOS-Chem model and their monthly variations (b) from 2010 to 2019.

ments over 2012–17, during which time the annual total emissions for both the R2 and R4 inversions increased by more than 35 Tg (49.25 Tg for R4 and 36.09 Tg for R2). Yin et al. (2021) also found the lowest annual total emission in 2012 and the highest in 2017 in the PYVAR-LMDz (1.9° × 3.75°) inversion system. Its 8-year increasing trend is about 4.1 Tg yr^{-2}, accounting for nearly 1% of the annual total emissions. On average, the first 8-year increase trends in our study are 7.04 Tg yr^{-2} and 5.15 Tg yr^{-2} in the R4 and R2, respectively, corresponding to annual increases of nearly 1.24% and 0.99%. Compared to R4 inversion, both the increasing trend and the percentage of total emissions in the R2 experiment are more consistent with the results of Yin et al. (2021).

Large discrepancies in annual total emissions between R4 and R2 can be observed in 2019. While *a posteriori* emissions in R2 continued to decrease after a peak in 2017, the emissions in R4 rebounded after decreasing in 2018. From

the monthly comparison shown in Fig. 3b, we found that the difference in 2019 arose mainly from the maximum emissions during summer. In addition to the large emissions gap in 2019, we found that emissions in summer (July in the NH and December in the SH) caused most of the difference in other years.

The latitudinal breakdown of emissions from 22 ensemble inversion results concluded by Saunois et al. (2020) reveals the dominance of tropical emissions at 368 Tg yr^{-1} [337–399], representing 64% of the global total over 2008–17. A total of 32% of the emissions are from the mid-latitudes (186 Tg yr^{-1} [166–204]), and 4% are from high latitudes (above 60°N). In this study, the dominant emissions over the tropics are 364.71 Tg yr^{-1} and 355.31 Tg yr^{-1} in R4 and R2, representing 63.64% and 62.48% of their global totals over 2010–19, respectively. Emissions from mid-latitudes account for 34.22% (196.12 Tg yr^{-1}) and 35.17% (200.02 Tg yr^{-1}). Those from high-latitude regions are 12.22 Tg yr^{-1} (2.13%) and 13.31 Tg yr^{-1} (2.34%) in R4 and R2, respectively. The emission distribution proportions in various latitudinal zonal are similar between R2 and R4 and are basically consistent with those given by Saunois et al. (2020). For the emission variation over various latitudinal zones, our results reveal global emission enhancements over 2015–19, compared to the first half of the 2010s, are derived mostly from tropical regions, representing 77.76% (21.57 Tg yr^{-1}) and 71.57% (15.85 Tg yr^{-1}) of their totals in R4 (27.74 Tg yr^{-1}) and R2 (22.11 Tg yr^{-1}). Compared to the R4 results, emission increases are more gradual in the R2 grid, with larger contributions coming from the mid-latitudes (9.28%) and high-latitudes (19.14%).

Considering the 1.16% larger proportion of tropical emissions to global totals, as well as the corresponding 6.19% greater contribution to the 5-year global increase in R4, we suggest explanations that may include a high-latitude bias in GEOS-Chem due to an imprecise description of convection across the tropopause (Bisht et al., 2021) and the inaccurate estimation of the vertical exchange between troposphere and stratosphere (Strahan and Polansky, 2006). Especially in R4, there is less methane in the troposphere and more methane in the lower stratosphere at high latitudes (shown in Fig. A3), which produces a latitudinal XCH_4 bias with large positive XCH_4 anomalies at high latitudes and small negative anomalies in the tropics (shown in Fig. A2). Bisht et al. (2021) attributed this bias to stronger quasi-horizontal mixing across the tropopause from the tropics to the mid-high latitudes in the model with a low resolution by comparing MIROC4-ACTM simulated CH_4 vertical profiles in the upper troposphere and lower stratosphere with the CONTRAIL (Comprehensive Observation Network for TRace gases by AIrLiner) aircraft observations. Stanevich et al. (2020) compared GEOS-Chem simulated XCH_4 in R4 and R2 with GOSAT, TCCON, and ACE-FTS (Atmospheric Chemistry Experiment Fourier Transform Spectrometer) observations and found that the R2 model produced a better simulation of CH_4, with smaller biases and a higher correlation to the independent data. They explained that the major reason for latitude-dependent errors is the excessive mixing in the upper troposphere and lower stratosphere at coarser resolutions. The larger model biases at R4 grid thus impact the distribution of *a posteriori* emissions and their long-term trends.

Detailed zonal mean *a posteriori* emissions variation by the R4 (a) and R2 (b) from 2010 to 2019 are presented in Fig. 4. We found the latitudinal distributions of the maximum values differ greatly in mid-latitude regions between R4 and R2. Compared with the single maximum around 35°N in R4, several additional high zonal mean values were obtained in R2, with the maximum near 30°N being the most apparent. Additionally, emissions around 25°N in R2 increased significantly in the 2010s, which was unclear in the R4 results. These results suggest that inversions using coarse models have difficulty reproducing hotspot emissions that are widely distributed over the mid-latitudes.

4.2. *Regional emissions comparison*

Decadal annual mean CH_4 emissions (shown in Fig. A5) are aggregated into the widely used 11 TransCom-3 land regions (Gurney et al., 2002), which are shown in Figure 5a. Among the eleven regions, the largest annual emissions from Eurasia Temperate are 123.28 Tg yr^{-1} and 135.70 Tg yr^{-1} in R4 and R2, accounting for 21.51% and 23.85% of their global totals, respectively. Annual emissions in R4 are underestimated by about 12.42 Tg yr^{-1} compared with those in R2, accounting for 9.15% of the regional totals. In the tropics, where wetlands are widely distributed, underestimations in annual emissions by R4 are about 5.85 Tg yr^{-1} in Tropical South America (58.97 Tg yr^{-1} for R4 and 64.81 Tg yr^{-1} for R2) and 8.70 Tg yr^{-1} in Tropical Asia (46.23 Tg yr^{-1} for R4 and 54.93 Tg yr^{-1} for R2), accounting for 9.02% and 15.84% of their annual totals. For North Africa, emissions in R4 are 3.46 Tg yr^{-1} higher than those in R2 (50.80 Tg yr^{-1} for R4 and 47.34 Tg yr^{-1}). For the high-latitude regions of Eurasia Boreal, North American Boreal, and Europe, the optimized emissions from R4 are smaller than emissions simulated by the R2 model. The differences between R4 and R2 are 2.19, 2.72, and 6.32 Tg yr^{-1}, accounting for 13.75%, 25.68%, and 15.67% of the totals in these regions, respectively.

In terms of differences in regional annual total emissions between the first half and the second half of the 2010s (shown in Fig. 5b), five-year annual total methane emissions in Eurasia Boreal, North Africa, and Tropical South America have shown significant growth (> 4 Tg yr^{-1}) compared to those over 2010–14. While the increase from Eurasia Boreal in the R4 inversion is smaller than that in R2, emission increases over North Africa and Tropical South America are overestimated in the R4. For emission growth inside the half-decade over the 2010s, we found increased emissions in North Africa (1.79 Tg yr^{-2} for R4 and 1.29 Tg yr^{-2} for R2, shown in Fig. 6f) and South American Temperate (1.08 Tg yr^{-2} for R4 and 1.21 Tg yr^{-2} for R2, shown in Fig. 6k) contribute the most (71.69% for R4 and 59.67% for R2) to global emissions growth (4.01 Tg yr^{-2} for R4 and

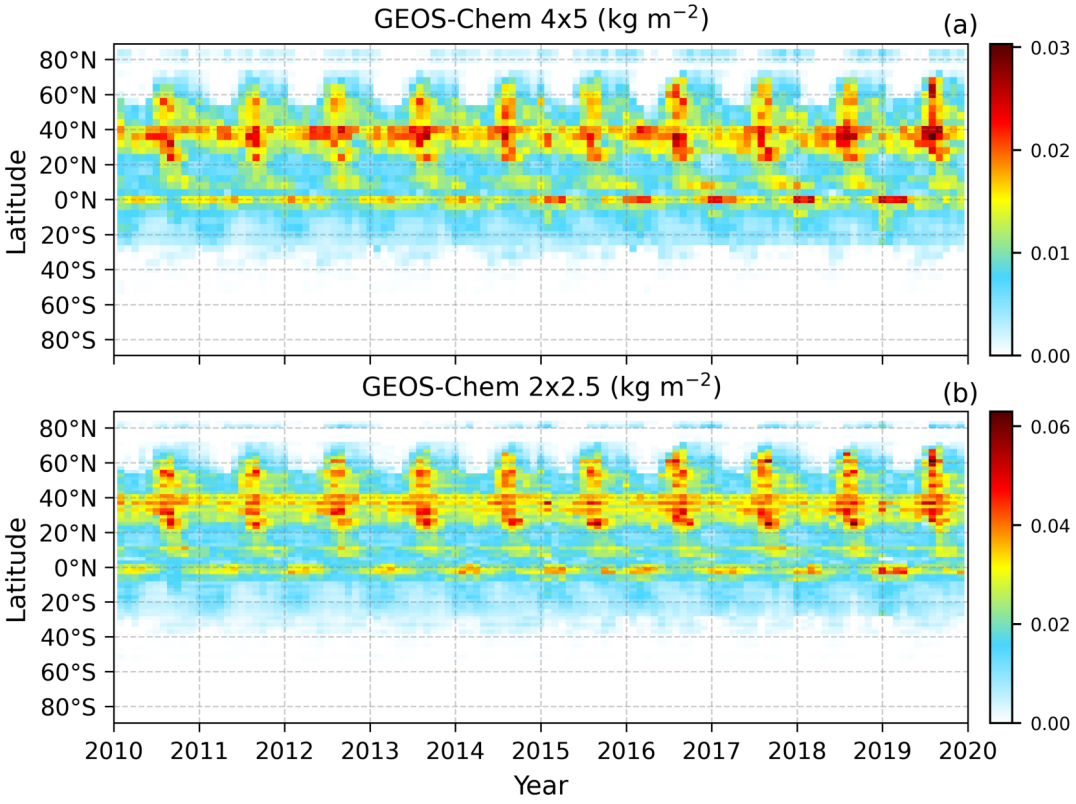

Fig. 4. Zonal mean monthly variations of methane emissions in the R4 (a) and R2 (b) versions of the GEOS-Chem model from 2010 to 2019.

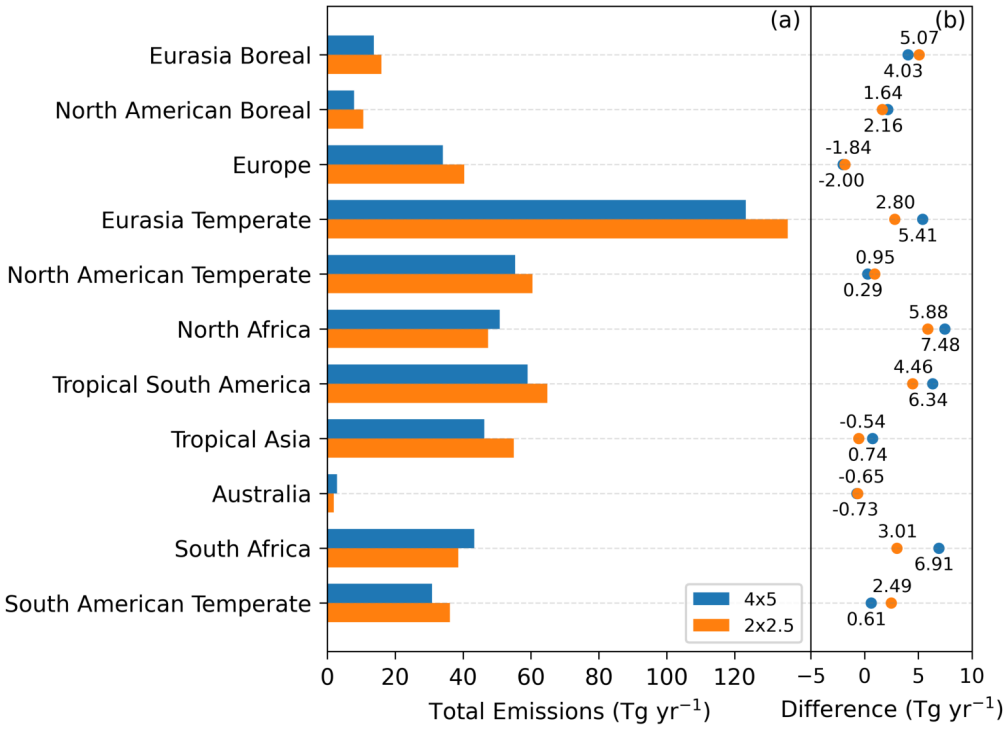

Fig. 5. Annual total methane emissions in the eleven TransCom-3 land regions from 2010 to 2019. Decadal annual mean optimized emissions obtained using the R4 (blue) and R2 (orange) versions of the GEOS-Chem model (a), and the differences in methane emissions between the second and the first half of the 2010s in R4 and R2 (b).

4.19 Tg yr^{-2} for R2) before 2015. From six ensemble mean results over 2010–18, using the inversion system PYVAR-LMDz, Yin et al. (2021) also concluded that methane emissions from Tropical Africa (a large part of North Africa and a small part of South Africa in this study) and Eastern Brazil (basically located in South American Temperate) show an upward trend since 2012. However, several inversion results summarized by Canadell et al. (2021) show increases in the first half of the 2010s mainly from Eurasia Temperate (including West Asia, East Asia, and South Asia) and North America Temperate. In our study, the main contributions to emissions growth from 2010 to 2014 occurred in North Africa (including Northern Africa and part of Central Africa) and South American Temperate (South part of Tropical America and Temperate South America), while only a slight emission increase could be found from Central Africa and Temperate America with no trend in South Africa and large interannual variation in Tropical America. During the second half of the 2010s, accelerated methane growth in the atmosphere was mainly due to emissions from the Eurasia Boreal (1.46 Tg yr^{-2} for R4 and 1.63 Tg yr^{-2} for R2, shown in Fig. 6a) and Tropical South America (1.72 Tg yr^{-2} for R4 and 1.43 Tg yr^{-2} for R2, shown in Fig. 6g). The interannual variation in Eurasia Boreal (Russia) from Yin et al. (2021) is coincident with the increased emissions which occurred in 2014 and peaked in 2016. Chandra et al. (2021) also reported a similar increasing trend over Eurasia Boreal (North Asia), with emissions reaching a maximum in 2016. Our study additionally shows that in 2019, emissions from the Eurasia Boreal continued growing after a decline in 2017 and were nearly twice the emissions in 2010. In Europe (Fig. 6c), there are decadal declining trends, with the average rates of decrease of –0.58 Tg yr^{-2} and –0.59 Tg yr^{-2} in R4 and R2, respectively, accounting for about –1.7% of their totals. This result is consistent with an ongoing consensus (Saunois et al., 2020; Canadell et al., 2021; Chandra et al., 2021; Stavert et al., 2022). For Australia (Fig. 6i), annual emissions in both R2 and R4 show decreasing trends. However, these results incur large uncertainties as the relative difference in the 5-year decreases reached more than half of the total emissions.

Over the second half of the 2010s, methane variations in the South America Temperate and South Africa differ greatly between R4 and R2. The result in R2 shows no obvious decreasing trend in South America Temperate and no substantial increase in South Africa, which is similar to the results from Yin et al. (2021) and Stavert et al. (2022). Therefore, emission growth in South Africa in R4 may be overestimated, and emission trends in South America Temperate are insufficiently estimated over 2015–19.

The half-decadal variation in Fig. 5b shows large discrepancies for the Eurasia Temperate. The mean annual emission increase compared to those from the first half of the 2010s in R4 (5.41 Tg yr^{-1}) is nearly twice that in R2 (2.80 Tg yr^{-1}), with large discrepancies over 2015–19 (Fig. 6d). While emissions in R4 show remarkable growth after fluctuating between 2012 and 2015, those in the R2 inversion show no consistent growth with a continuous fluctu-

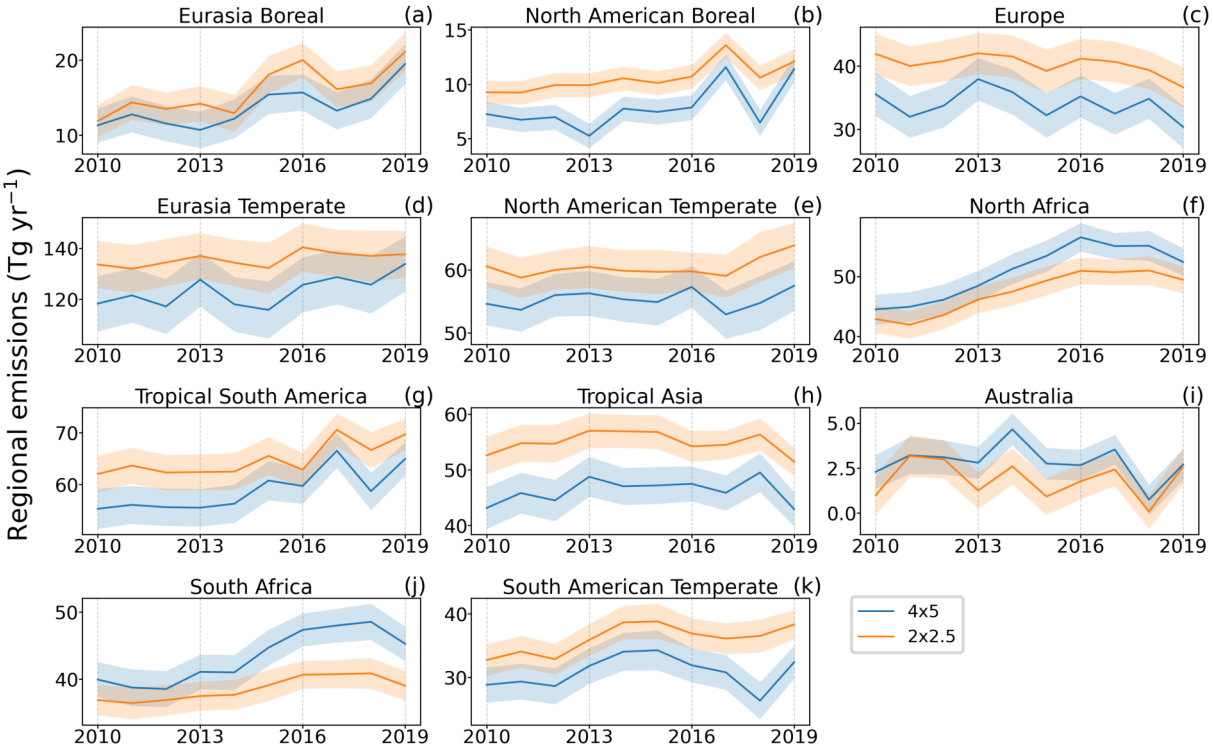

Fig. 6. Regional methane emission trends in the eleven TransCom-3 land regions (a–k) in R4 (blue) and R2 (orange) inversions and their monthly variations (b) from 2010 to 2019.

ation in the following years. There is also an ongoing debate about emissions from Eurasia Temperate among studies, which mainly focus on China, though all of them agree that coal emission has been overestimated by the widely used EDGAR (Maasakkers et al., 2019; Miller et al., 2019; Lu et al., 2021; Yin et al., 2021; Zhang et al., 2021; Stavert et al., 2022). Miller et al. (2019), Maasakkers et al. (2019), and Chandra et al. (2021) attributed atmospheric methane growth from 2010 to 2015 to increased emissions, partly from China, related to fossil fuel exploration. Stavert et al. (2022) and Yin et al. (2021) suggested a substantial increase in Chinese anthropogenic methane emissions from fossil fuels, agriculture, and waste from 2010 to 2017. However, Lu et al. (2021) compared inversion results using various observations, and found that anthropogenic emission trends in China for GOSAT-only (–0.6 Tg yr $^{-2}$) and for GOSAT and in situ joint inversion (–0.4 Tg yr $^{-2}$) over 2010–2017. Zhang et al. (2021) concluded that anthropogenic emission trends in China peaked midway within the 2010–18 record. One possible reason for the discrepancy in their inversion results may be the large uncertainties involved in the distribution of a priori estimates. While some studies suggest a decline in Chinese coal mining emissions since 2012 (Sheng et al., 2019, 2021; Gao et al., 2020, 2021), the trend reported by Lin et al. (2021) using national-level activity data from the National Bureau of Statistics of China and localized emission factors showed a slight increasing trend of 0.5 Tg yr $^{-2}$ for the period 2015–19. Additionally, the tropospheric transport bias involved in the coarser model may be another important reason (Stanevich et al., 2020). Stanevich et al. (2021) found that resolution-dependent model errors in the stratosphere can be traced back to biases in the uplift of CH_4 over the source regions in eastern China and North America. Regarding observational errors in GOSAT retrievals, Huang et al. (2020) found aerosols with a high single-scattering albedo and low asymmetry parameters (such as water-soluble aerosols, highly loaded in Northern China) induce large biases in the retrieval. Besides, there are very few retrievals over Southern China during the summer/monsoon season because of cloud cover (Chandra et al., 2017). Both the quality and the coverage of GOSAT XCH_4 retrievals may affect the convergence of posterior emissions in inversion.

To further study the systematic discrepancies in regional emissions, we used a box plot to show the difference between R4 and R2 on a finer monthly scale in Fig. 7. Despite similar long-term trends that can be found in most regions, there are large discrepancies between R4 and R2 on monthly timescales. Interquartile Range (IR = Q3 – Q1) relative to their monthly emissions is larger than 30% in Eura-

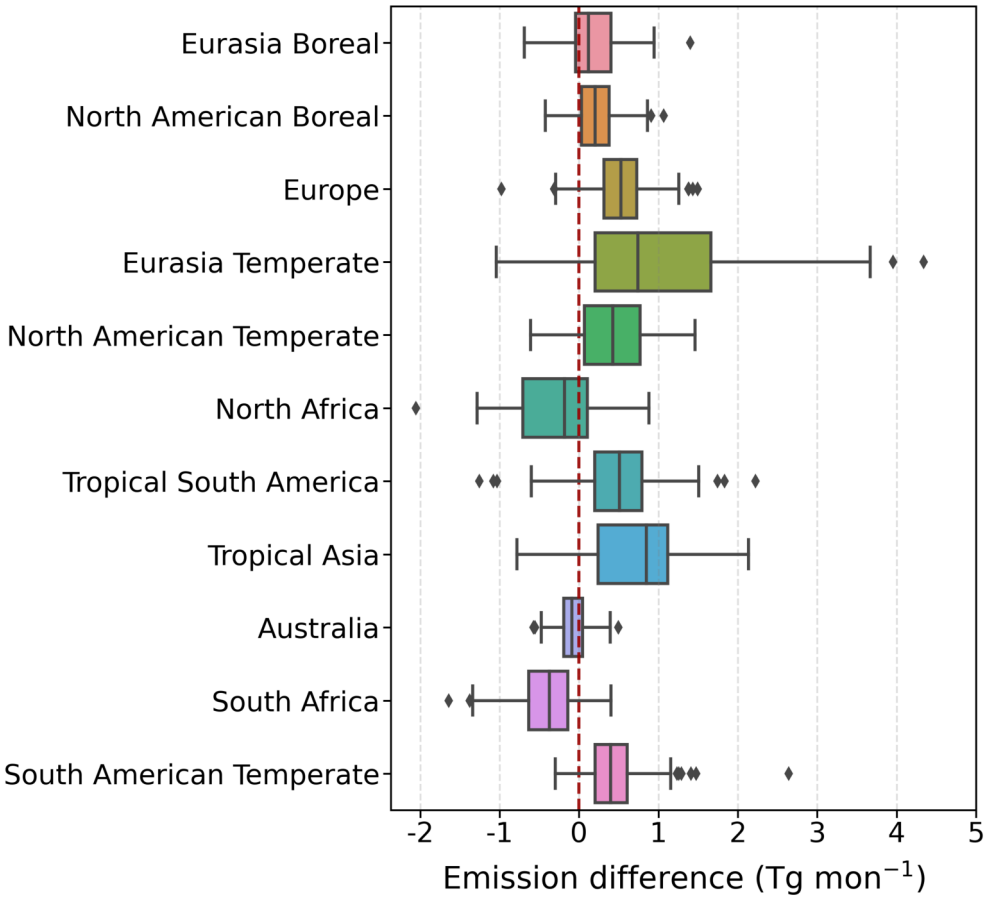

Fig. 7. Box diagram (minimum, maximum, median, first quartile, and third quartile) of regional monthly methane emissions difference (R2 minus R4) in the eleven TransCom-3 land regions.

sia, North American Boreal, and Australia, with the largest values in Australia at 105%. In other regions, IR values range from 10% to 20% of their monthly mean emissions, indicating that the horizontal resolution of CTMs can profoundly impact regional emission variation on monthly timescales. Therefore, monthly variations of regional methane emissions have large uncertainties and should be interpreted with caution.

5. Conclusions

To evaluate long-term methane emission trends using CTMs with coarse horizontal resolutions, we used the EnKF framework to optimize a priori methane emission inventories in the 4° × 5° (R4) and 2° × 2.5° (R2) versions of GEOS-Chem by assimilating GOSAT proxy v9.0 retrievals and compared the inverted emissions and their long-term trends from 2010 to 2019 on global, latitudinal, and regional scales.

Global annual total methane emissions in R4 and R2 during the 2010s are 573.04 Tg yr^{-1} and 568.63 Tg yr^{-1}, respectively, within the range of 22 top-down ensemble results (576 Tg yr^{-1} [550–594]) given by the Global Carbon Project (Saunois et al., 2020). Most increases were derived from enhancements over 2012–17, with the largest growth in 2013 (25.51 Tg yr^{-2} in R4 and 13.00 Tg yr^{-2} in R2). Compared to R4, the trend in R2 is closer to the ensemble mean trend (nearly 1%) inverted by Yin et al. (2021). Discrepancies between the two inversions mainly arise from different emissions during the boreal summer.

The latitudinal breakdown of emissions indicates that the dominant emissions over the tropics are 364.71 Tg yr^{-1} in R4 inversion and 355.31 Tg yr^{-1} in R2 inversion, representing 63.64% and 62.48% of their global totals over 2010–19, respectively. Both are well within the range of tropical emissions (368 Tg yr^{-1} [337–399]) reported by Saunois et al. (2020). Compared to the R2 model, the inversion based on R4 tends to overestimate tropical emissions (by 13.3 Tg yr^{-1}) and their contribution to the global half-decadal increase (by 6.19%), which is accompanied by a general underestimation (by 8.9 Tg yr^{-1}) in the extratropics. These differences may be caused by errors in modeling the vertical exchange between the troposphere and stratosphere in high latitudes (Strahan and Polansky, 2006; Stanevich et al., 2020) in the R4, and, to a lesser extent, in the R2 .

Among the eleven TransCom-3 land regions, similar trends with systematic discrepancies can be found in most regions for long-term variations, especially during the first half of the 2010s. Compared with mean emissions over the first five years of the 2010s, increases in mean emissions over 2015–19 mainly came from Eurasia Boreal, North Africa, South America Temperate, and Tropical South America, of which North Africa (1.79 Tg yr^{-2} for R4 and 1.29 Tg yr^{-2} for R2) and South America Temperate (1.08 Tg yr^{-2} for R4 and 1.21 Tg yr^{-2}) contributed the most (71.69% for R4 and 59.67% for R2) to the growth of global emissions from 2010 to 2014. During the second half of the 2010s, accelerated atmospheric increases in methane levels were mainly driven by Eurasia Boreal and Tropical South America emissions. Europe's annual methane emissions decreased by about –1.7% on both grids. Emission variations in Eurasia Temperate involve large uncertainties. The debate also exists among studies that mainly focus on China (Lu et al., 2021; Yin et al., 2021; Zhang et al., 2021; Stavert et al., 2022). The possible reasons may be large uncertainties involved in the distribution of a priori estimates (Gao et al., 2021; Lin et al., 2021), transport bias in the troposphere in CTMs (Stanevich et al., 2020, 2021), and sparse distribution of satellite retrievals (Chandra et al., 2017; Huang et al., 2020).

With ongoing and rapid increases in computing resources, atmospheric chemistry and transport models with higher resolution will be widely adopted; therefore, more atmospheric measurement data with consistent high spatial resolution will be needed. As several remote sensing retrieval products from various satellites are available (such as GOSAT, Tropomi, and MethaneSAT), methods to reasonably combine these products (such as taking advantage of the high accuracy of GOSAT retrievals and high spatial resolution of Tropomi retrievals) for inversion require further research.

Acknowledgements. This work is supported by the National Key R&D Plan of China (Grant No. SQ2019YFE013078), the Key Research Program of the Chinese Academy of Sciences (Grant No. ZDRW-ZS-2019-1), and the National Key R&D Program of China (Grant No. 2017YFB0504000). The support provided by the China Scholarship Council (CSC) and the University of Chinese Academy of Sciences during a visit of Sihong ZHU to the University of Edinburgh are also acknowledged. We thank Professor Paul Palmer for his useful comments. We thank the individual investigators who collected XCO_2 and XCH_4 data as part of the Total Carbon Column Observing Network (TCCON). We thank the broader GOSAT team, who provided their L1 data to develop the proxy CH_4 data product. We also thank the GEOS-Chem community, particularly the team at Harvard who helped maintain the GEOS-Chem model and the NASA Global Modeling and Assimilation Office (GMAO), who provided the MERRA 2 data product.

APPENDIX

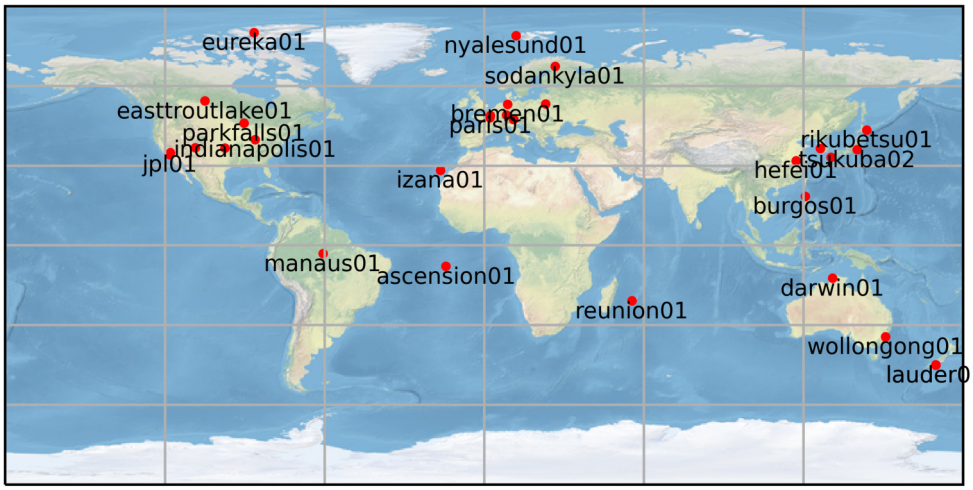

Fig. A1. Geographic locations of observation sites in the TCCON network.

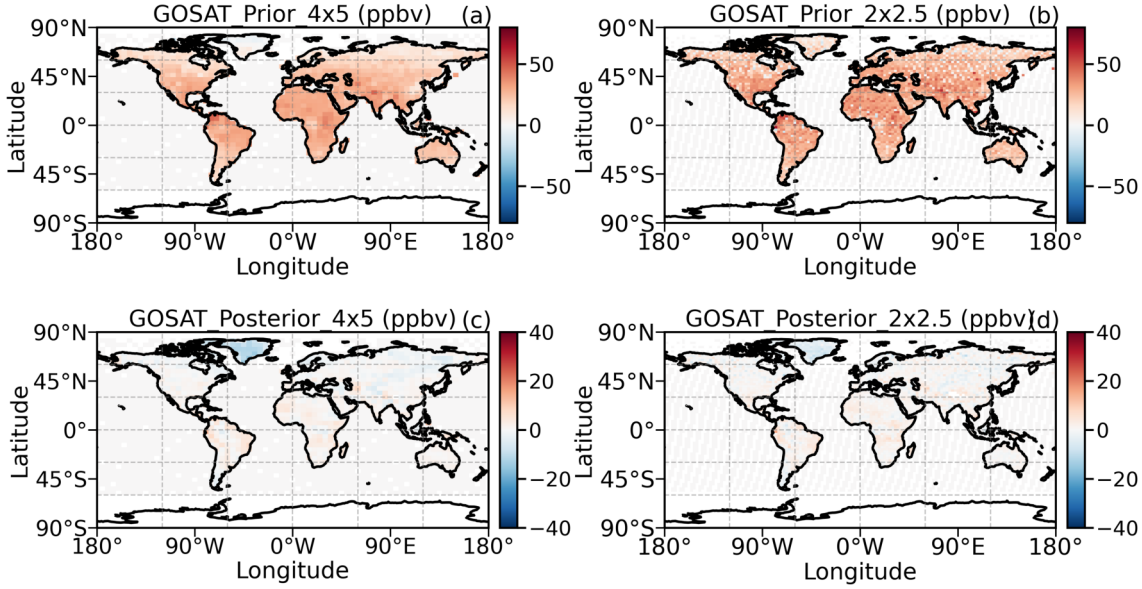

Fig. A2. The decadal mean difference between GOSAT-retrieved methane column concentrations (XCH_4) and those simulated using GEOS-Chem with a priori emissions at R4 (a) and R2 (b) scales and using *a posteriori* emissions after inversion at grid scales of R4 (c) and R2 (d).

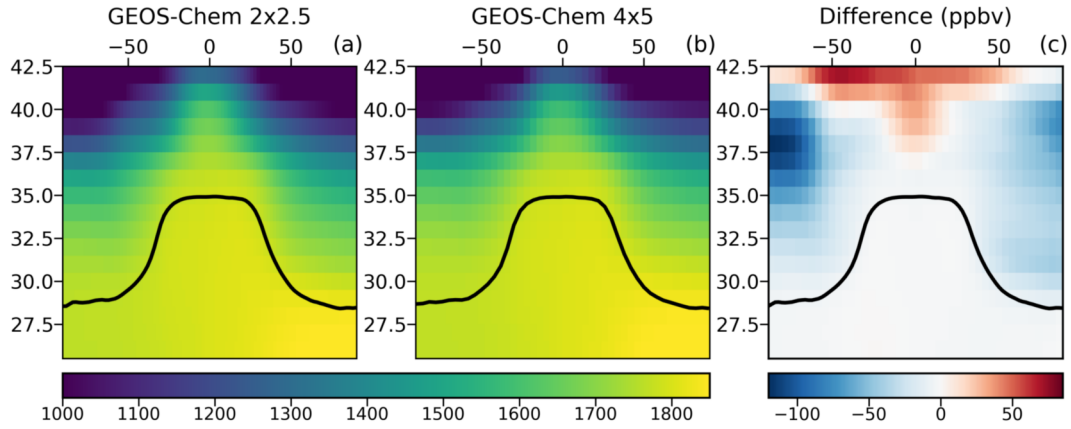

Fig. A3. The decadal zonal mean of the 3-D methane concentration field in R2 (a) and R4 (b) versions of the GEOS-Chem model and their difference (R2 minus R4) (c).

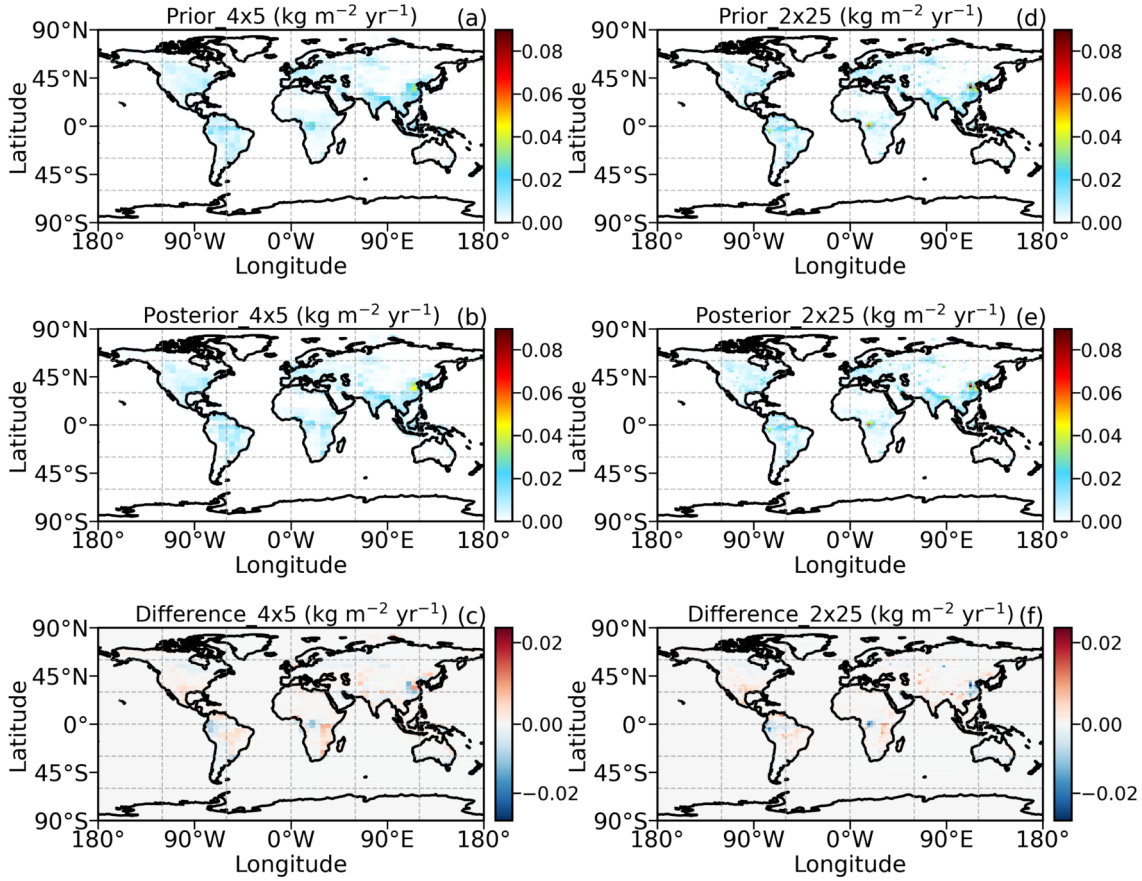

Fig. A4. Decadal mean distribution of a priori and a posteriori methane emissions in using R4 (a, d) and the R2 (b, e) inversions and their differences (a posteriori minus a priori) (c, f).

REFERENCES

Bisht, J. S. H., and Coauthors, 2021: Seasonal variations of SF_6, CO_2, CH_4, and N_2O in the UT/LS region due to emissions, transport, and chemistry. *J. Geophys. Res.*, **126**(4), e2020JD033541, https://doi.org/10.1029/2020JD033541.

Bloom, A. A., P. I. Palmer, A. Fraser, D. S. Reay, and C. Frankenberg, 2010: Large-scale controls of methanogenesis inferred from methane and gravity spaceborne data. *Science*, **327**, 322–325, https://doi.org/10.1126/science.1175176.

Bloom, A. A., and Coauthors, 2017: A global wetland methane emissions and uncertainty dataset for atmospheric chemical transport models (WetCHARTs version 1.0). *Geoscientific Model Development*, **10**, 2141–2156, https://doi.org/10.5194/gmd-10-2141-2017.

Bosilovich, M. G., R. Lucchesi, and M. Suarez, 2016: MERRA-2: File specification. GMAO Office Note No.9 (Version 1.1), 73 pp.

Bousquet, P., and Coauthors, 2006: Contribution of anthropogenic and natural sources to atmospheric methane variability. *Nature*, **443**, 439–443, https://doi.org/10.1038/nature05132.

Bousserez, N., D. K. Henze, B. Rooney, A. Perkins, K. J. Wecht, A. J. Turner, V. Natraj, and J. R. Worden, 2016: Constraints on methane emissions in North America from future geostationary remote-sensing measurements. *Atmospheric Chemistry and Physics*, **16**, 6175–6190, https://doi.org/10.5194/acp-16-6175-2016.

Brasseur, G. P., and D. J. Jacob, 2017: *Modeling of Atmospheric Chemistry*. Cambridge University Press.

Canadell, J. G., and Coauthors, 2021: Global carbon and other biogeochemical cycles and feedbacks. *Climate Change 2021: The Physical Science Basis. Contribution of Working Group I to the Sixth Assessment Report of the Intergovernmental Panel on Climate Change*, V. Masson-Delmotte et al., Eds., Cambridge University Press.

Chandra, N., S. Hayashida, T. Saeki, and P. K. Patra, 2017: What controls the seasonal cycle of columnar methane observed by GOSAT over different regions in India? *Atmospheric Chemistry and Physics*, **17**(20), 12 633–12 643, https://doi.org/10.5194/acp-17-12633-2017.

Chandra, N., and Coauthors, 2021: Emissions from the oil and gas sectors, coal mining and ruminant farming drive methane growth over the past three decades. *J. Meteor. Soc. Japan.*, **99**(2), 309–337, https://doi.org/10.2151/jmsj.2021-015.

Darmenov, A., and da Silva, A. M., 2013: The quick fire emissions dataset (QFED)—Documentation of versions 2.1, 2.2 and 2.4. NASA Tech. Rep. Series on Global Modeling and Data Assimilation, NASA TM-2013-104606.

Etiope, G., 2015: *Natural Gas Seepage*: *The Earth's Hydrocarbon Degassing*. Springer.

Etminan, M., G. Myhre, E. J. Highwood, and K. P. Shine, 2016: Radiative forcing of carbon dioxide, methane, and nitrous oxide: A significant revision of the methane radiative forcing. *Geophys. Res. Lett.*, **43**, 12 614–12 623, https://doi.org/10.1002/2016GL071930.

Feng, L., P. I. Palmer, H. Bösch, and S. Dance, 2009: Estimating surface CO_2 fluxes from space-borne CO_2 dry air mole fraction observations using an ensemble Kalman Filter. *Atmospheric Chemistry and Physics*, **9**(8), 2619–2633, https://doi.org/10.5194/acp-9-2619-2009.

Feng, L., and Coauthors, 2017: Consistent regional fluxes of CH_4 and CO_2 inferred from GOSAT proxy XCH_4: XCO_2 retrievals, 2010–2014. *Atmospheric Chemistry and Physics*, **17**, 4781–4797, https://doi.org/10.5194/acp-17-4781-2017.

Frankenberg, C., I. Aben, P. Bergamaschi, E. J. Dlugokencky, R. van Hees, S. Houweling, P. van der Meer, R. Snel, and P. Tol, 2011: Global column-averaged methane mixing ratios from 2003 to 2009 as derived from SCIAMACHY: Trends and variability. *J. Geophys. Res.*, **116**, D04302, https://doi.org/10.1029/2010JD014849.

Fraser, A., and Coauthors, 2013: Estimating regional methane surface fluxes: The relative importance of surface and GOSAT mole fraction measurements. *Atmospheric Chemistry and Physics*, **13**, 5697–5713, https://doi.org/10.5194/acp-13-5697-2013.

Fraser, A., P. I. Palmer, L. Feng, H. Bösch, R. Parker, E. J. Dlugokencky, P. B. Krummel, and R. L. Langenfelds, 2014: Estimating regional fluxes of CO_2 and CH_4 using space-borne observations of XCH_4:XCO_2. *Atmospheric Chemistry and Physics*, **14**, 12 883–12 895, https://doi.org/10.5194/acp-14-12883-2014.

Fung, I., J. John, J. Lerner, E. Matthews, M. Prather, L. P. Steele, and P. J. Fraser, 1991: Three-dimensional model synthesis of the global methane cycle. *J. Geophys. Res.*, **96**, 13 033–13 065, https://doi.org/10.1029/91JD01247.

Ganesan, A. L., and Coauthors, 2019: Advancing scientific understanding of the global methane budget in support of the Paris Agreement. *Global Biogeochemical Cycles*, **33**, 1475–1512, https://doi.org/10.1029/2018GB006065.

Gao, J. L., C. H. Guan, and B. Zhang, 2020: China's CH_4 emissions from coal mining: A review of current bottom-up inventories. *Science of the Total Environment*, **725**, 138295, https://doi.org/10.1016/j.scitotenv.2020.138295.

Gao, J. L., C. H. Guan, B. Zhang, and K. Li, 2021: Decreasing methane emissions from China's coal mining with rebounded coal production. *Environmental Research Letters*, **16**(12), 124037, https://doi.org/10.1088/1748-9326/ac38d8.

Gurney, K. R., and Coauthors, 2002: Towards robust regional estimates of CO_2 sources and sinks using atmospheric transport models. *Nature*, **415**(6872), 626–630, https://doi.org/10.1038/415626a.

Huang, Y. X., V. Natraj, Z.-C. Zeng, P. Kopparla, and Y. L. Yung, 2020: Quantifying the impact of aerosol scattering on the retrieval of methane from airborne remote sensing measurements. *Atmospheric Measurement Techniques*, **13**(12), 6755–6769, https://doi.org/10.5194/amt-13-6755-2020.

Jacob, D. J., and Coauthors, 2016: Satellite observations of atmospheric methane and their value for quantifying methane emissions. *Atmospheric Chemistry and Physics*, **16**, 14 371–14 396, https://doi.org/10.5194/acp-16-14371-2016.

Janardanan, R., and Coauthors, 2020: Country-scale analysis of methane emissions with a high-resolution inverse model using GOSAT and surface observations. *Remote Sensing*, **12**(3), 375, https://doi.org/10.3390/rs12030375.

Janssens-Maenhout, G., and Coauthors, 2019: EDGAR v4.3.2 global atlas of the three major greenhouse gas emissions for the period 1970–2012. *Earth System Science Data*, **11**, 959–1002, https://doi.org/10.5194/essd-11-959-2019.

Karion, A., C. Sweeney, P. Tans, and T. Newberger, 2010: AirCore: An innovative atmospheric sampling system. *J. Atmos. Oceanic Technol.*, **27**, 1839–1853, https://doi.org/10.1175/2010JTECHA1448.1.

Kirschke, S., and Coauthors, 2013: Three decades of global methane sources and sinks. *Nature Geoscience*, **6**, 813–823, https://doi.org/10.1038/ngeo1955.

Kvenvolden, K. A., and B. W. Rogers, 2005: Gaia's breath—global methane exhalations. *Marine and Petroleum Geology*, **22**, 579–590, https://doi.org/10.1016/j.marpetgeo.2004.08.004.

Lin, J.-T., and M. B. McElroy, 2010: Impacts of boundary layer mixing on pollutant vertical profiles in the lower troposphere: Implications to satellite remote sensing. *Atmos. Environ.*, **44**, 1726–1739, https://doi.org/10.1016/j.atmosenv.2010.02.009.

Lin, X. H., W. Zhang, M. Crippa, S. S. Peng, P. F. Han, N. Zeng, L. J. Yu, and G. C. Wang, 2021: A comparative study of anthropogenic CH_4 emissions over China based on the ensembles of bottom-up inventories. *Earth System Science Data*, **13**(3), 1073–1088, https://doi.org/10.5194/essd-13-1073-2021.

Locatelli, R., and Coauthors, 2013: Impact of transport model errors on the global and regional methane emissions estimated by inverse modelling. *Atmospheric Chemistry and Physics*, **13**(19), 9917–9937, https://doi.org/10.5194/acp-13-9917-2013.

Locatelli, R., P. Bousquet, M. Saunois, F. Chevallier, and C. Cressot, 2015: Sensitivity of the recent methane budget to LMDz sub-grid-scale physical parameterizations. *Atmospheric Chemistry and Physics*, **15**, 9765–9780, https://doi.org/10.5194/acp-15-9765-2015.

Lu, X., and Coauthors, 2021: Global methane budget and trend, 2010–2017: Complementarity of inverse analyses using in situ (GLOBALVIEWplus CH_4 ObsPack) and satellite (GOSAT) observations. *Atmospheric Chemistry and Physics*, **21**, 4637–4657, https://doi.org/10.5194/acp-21-4637-2021.

Lunt, M. F., P. I. Palmer, L. Feng, C. M. Taylor, H. Boesch, and R. J. Parker, 2019: An increase in methane emissions from tropical Africa between 2010 and 2016 inferred from satellite data. *Atmospheric Chemistry and Physics*, **19**, 14 721–14 740, https://doi.org/10.5194/acp-19-14721-2019.

Lunt, M. F., P. I. Palmer, A. Lorente, T. Borsdorff, J. Landgraf, R. J. Parker, and H. Boesch, 2021: Rain-fed pulses of methane from East Africa during 2018–2019 contributed to atmospheric growth rate. *Environmental Research Letters*, **16**(2), 024021, https://doi.org/10.1088/1748-9326/abd8fa.

Lyon, D. R., and Coauthors, 2015: Constructing a spatially resolved methane emission inventory for the Barnett Shale region. *Environ. Sci. Technol.*, **49**, 8147–8157, https://doi.org/10.1021/es506359c.

Maasakkers, J. D., and Coauthors, 2016: Gridded national inventory of U.S. methane emissions. *Environ. Sci. Technol.*, **50**, 13 123–13 133, https://doi.org/10.1021/acs.est.6b02878.

Maasakkers, J. D., and Coauthors, 2019: Global distribution of methane emissions, emission trends, and OH concentrations and trends inferred from an inversion of GOSAT satellite data for 2010–2015. *Atmospheric Chemistry and Physics*, **19**, 7859–7881, https://doi.org/10.5194/acp-19-7859-2019.

Meirink, J. F., P. Bergamaschi, and M. C. Krol, 2008: Four-dimensional variational data assimilation for inverse modelling of

atmospheric methane emissions: Method and comparison with synthesis inversion. *Atmospheric Chemistry and Physics*, **8**, 6341–6353, https://doi.org/10.5194/acp-8-6341-2008.

Melton, J. R., and Coauthors, 2013: Present state of global wetland extent and wetland methane modelling: Conclusions from a model inter-comparison project (WETCHIMP). *Biogeosciences*, **10**, 753–788, https://doi.org/10.5194/bg-10-753-2013.

Miller, S. M., A. M. Michalak, R. G. Detmers, O. P. Hasekamp, L. M. P. Bruhwiler, and S. Schwietzke, 2019: China's coal mine methane regulations have not curbed growing emissions. *Nature Communications*, **10**, 303, https://doi.org/10.1038/s41467-018-07891-7.

Murray, L. T., D. J. Jacob, J. A. Logan, R. C. Hudman, and W. J. Koshak, 2012: Optimized regional and interannual variability of lightning in a global chemical transport model constrained by LIS/OTD satellite data. *J. Geophys. Res.*, **117**, D20307, https://doi.org/10.1029/2012JD017934.

Myhre, G., and Coauthors, 2013: Radiative forcing of the direct aerosol effect from AeroCom Phase II simulations. *Atmospheric Chemistry and Physics*, **13**, 1853–1877, https://doi.org/10.5194/acp-13-1853-2013.

Pandey, S., and Coauthors, 2019: Influence of atmospheric transport on estimates of variability in the global methane burden. *Geophys. Res. Lett.*, **46**(4), 2302–2311, https://doi.org/10.1029/2018GL081092.

Parker, R., and Coauthors, 2011: Methane observations from the Greenhouse Gases Observing SATellite: Comparison to ground-based TCCON data and model calculations. *Geophys. Res. Lett.*, **38**(15), L15807, https://doi.org/10.1029/2011GL047871.

Parker, R. J., and Coauthors, 2015: Assessing 5 years of GOSAT Proxy XCH_4 data and associated uncertainties. *Atmospheric Measurement Techniques*, **8**(11), 4785–4801, https://doi.org/10.5194/amt-8-4785-2015.

Parker, R. J., and Coauthors, 2020: A decade of GOSAT proxy satellite CH_4 observations. *Earth System Science Data Discussions*, **2020**, 1–36, https://doi.org/10.5194/essd-2020-114.

Parker R J, and Coauthors., 2020: A decade of GOSAT Proxy satellite CH 4 observations. *Earth System Science Data*, **12**(4), 3383–3412, https://doi.org/10.5194/essd-12-3383-2020.

Patra, P. K., and Coauthors, 2011: TransCom model simulations of CH_4 and related species: Linking transport, surface flux and chemical loss with CH_4 variability in the troposphere and lower stratosphere. *Atmospheric Chemistry and Physics*, **11**, 12 813–12 837, https://doi.org/10.5194/acp-11-12813-2011.

Prather, M. J., C. D. Holmes, and J. Hsu, 2012: Reactive greenhouse gas scenarios: Systematic exploration of uncertainties and the role of atmospheric chemistry. *Geophys. Res. Lett.*, **39**(9), L09803, https://doi.org/10.1029/2012gl051440.

Ridgwell, A. J., S. J. Marshall, and K. Gregson, 1999: Consumption of atmospheric methane by soils: A process-based model. *Global Biogeochemical Cycles*, **13**, 59–70, https://doi.org/10.1029/1998GB900004.

Saito, R., and Coauthors, 2013: TransCom model simulations of methane: Comparison of vertical profiles with aircraft measurements. *J. Geophys. Res.*, **118**, 3891–3904, https://doi.org/10.1002/jgrd.50380.

Saunois, M., and Coauthors, 2020: The global methane budget: 2000–2017. *Earth System Science Data*, **12**(3), 1561–1623, https://doi.org/10.5194/essd-12-1561-2020.

Schaefer, H., 2019: On the causes and consequences of recent trends in atmospheric methane. *Current Climate Change Reports*, **5**, 259–274, https://doi.org/10.1007/s40641-019-00140-z.

Schaefer, H., and Coauthors, 2016: A 21st-century shift from fossil-fuel to biogenic methane emissions indicated by $^{13}CH_4$. *Science*, **352**, 80–84, https://doi.org/10.1126/science.aad2705.

Sheng, J.-X., D. J. Jacob, J. D. Maasakkers, M. P. Sulprizio, D. Zavala-Araiza, and S. P. Hamburg, 2017: A high-resolution (0.1°×0.1°) inventory of methane emissions from Canadian and Mexican oil and gas systems. *Atmos. Environ.*, **158**, 211–215, https://doi.org/10.1016/j.atmosenv.2017.02.036.

Sheng, J. X., S. J. Song, Y. Z. Zhang, R. G. Prinn, and G. Janssens-Maenhout, 2019: Bottom-up estimates of coal mine methane emissions in China: A gridded inventory, emission factors, and trends. *Environmental Science & Technology Letters*, **6**(8), 473–478, https://doi.org/10.1021/acs.estlett.9b00294.

Sheng, J. X., and Coauthors, 2021: Sustained methane emissions from China after 2012 despite declining coal production and rice-cultivated area. *Environmental Research Letters*, **16**(10), 104018, https://doi.org/10.1088/1748-9326/ac24d1.

Sherwen, T., and Coauthors, 2016: Global impacts of tropospheric halogens (Cl, Br, I) on oxidants and composition in GEOS-Chem. *Atmospheric Chemistry and Physics*, **16**(18), 12 239–12 271, https://doi.org/10.5194/acp-16-12239-2016.

Shindell, D., and Coauthors, 2012: Simultaneously mitigating near-term climate change and improving human health and food security. *Science*, **335**, 183–189, https://doi.org/10.1126/science.1210026.

Stanevich, I., and Coauthors, 2020: Characterizing model errors in chemical transport modeling of methane: Impact of model resolution in versions v9-02 of GEOS-Chem and v35j of its adjoint model. *Geoscientific Model Development*, **13**, 3839–3862, https://doi.org/10.5194/gmd-13-3839-2020.

Stanevich, I., and Coauthors, 2021: Characterizing model errors in chemical transport modeling of methane: Using GOSAT XCH_4 data with weak-constraint four-dimensional variational data assimilation. *Atmospheric Chemistry and Physics*, **21**, 9545–9572, https://doi.org/10.5194/acp-21-9545-2021.

Stavert, A. R., and Coauthors, 2022: Regional trends and drivers of the global methane budget. *Global Change Biology*, **28**(1), 182–200, https://doi.org/10.1111/gcb.15901.

Strahan, S. E., and B. C. Polansky, 2006: Meteorological implementation issues in chemistry and transport models. *Atmospheric Chemistry and Physics*, **6**(10), 2895–2910, https://doi.org/10.5194/acp-6-2895-2006.

Turner, A. J., and Coauthors, 2015: Estimating global and North American methane emissions with high spatial resolution using GOSAT satellite data. *Atmospheric Chemistry and Physics*, **15**, 7049–7069, https://doi.org/10.5194/acp-15-7049-2015.

Turner, A. J., D. J. Jacob, J. Benmergui, J. Brandman, L. White, and C. A. Randles, 2018: Assessing the capability of different satellite observing configurations to resolve the distribution of methane emissions at kilometer scales. *Atmospheric Chemistry and Physics*, **18**, 8265–8278, https://doi.org/10.5194/acp-18-8265-2018.

Webb, A. J., and Coauthors, 2016: CH_4 concentrations over the Amazon from GOSAT consistent with in situ vertical profile data. *J. Geophys. Res.*, **121**, 11 006–11 020, https://doi.org/

10.1002/2016JD025263.

Wecht, K. J., D. J. Jacob, M. P. Sulprizio, G. W. Santoni, S. C. Wofsy, R. Parker, H. Bösch, and J. Worden, 2014: Spatially resolving methane emissions in California: Constraints from the CalNex aircraft campaign and from present (GOSAT, TES) and future (TROPOMI, geostationary) satellite observations. *Atmospheric Chemistry and Physics*, **14**, 8173–8184, https://doi.org/10.5194/acp-14-8173-2014.

Wunch, D., and Coauthors, 2011: The total carbon column observing network. *Philosophical Transactions of the Royal Society A: Mathematical, Physical and Engineering Sciences*, **369**, 2087–2112, https://doi.org/10.1098/rsta.2010.0240.

Yin, Y., and Coauthors, 2021: Accelerating methane growth rate from 2010 to 2017: Leading contributions from the tropics and East Asia. *Atmospheric Chemistry and Physics*, **21**(16), 12 631–12 647, https://doi.org/10.5194/acp-21-12631-2021.

Yu, K. R., C. A. Keller, D. J. Jacob, A. M. Molod, S. D. Eastham, and M. S. Long, 2018: Errors and improvements in the use of archived meteorological data for chemical transport modeling: An analysis using GEOS-Chem v11-01 driven by GEOS-5 meteorology. *Geoscientific Model Development*, **11**(1), 305–319, https://doi.org/10.5194/gmd-11-305-2018.

Zhang, Y. Z., D. J. Jacob, J. D. Maasakkers, M. P. Sulprizio, J.-X. Sheng, R. Gautam, and J. Worden, 2018: Monitoring global tropospheric OH concentrations using satellite observations of atmospheric methane. *Atmospheric Chemistry and Physics*, **18**, 15 959–15 973, https://doi.org/10.5194/acp-18-15959-2018.

Zhang, Y. Z., and Coauthors, 2021: Attribution of the accelerating increase in atmospheric methane during 2010–2018 by inverse analysis of GOSAT observations. *Atmospheric Chemistry and Physics*, **21**, 3643–3666, https://doi.org/10.5194/acp-21-3643-2021.

Zhao Y. H., and Coauthors, 2020: Influences of hydroxyl radicals (OH) on top-down estimates of the global and regional methane budgets. *Atmospheric Chemistry and Physics*, **20**(15), 9525–9546, https://doi.org/10.5194/acp-20-9525-2020.